Low-power Optical Traps Using Anisotropic Metasurfaces: Asymmetric Potential Barriers and Broadband Response

N.K. Paul● and J.S. Gomez-Diaz*

Department of Electrical and Computer Engineering, University of California Davis, One Shields Avenue, Kemper Hall 2039, Davis, California 95616, USA

We propose lateral optical trapping of Rayleigh particles using tailored anisotropic and hyperbolic metasurfaces illuminated with a linearly polarized Gaussian beam. This platform permits optical traps to be engineered at the beam axis with a response governed by nonconservative and giant lateral recoil force coming from the directional excitation of confined surface plasmons during the light-scattering process. Compared to optical traps set over uniform metals, either in bulk or thin-layer configurations, the proposed traps are broadband in the sense that they can be set with beams oscillating at any frequency within a wide range in which the metasurface supports surface plasmons. Over that range, the metasurface dispersion evolves from an anisotropic elliptic to a hyperbolic regime going through a topological transition and enables optical traps with distinctive spatially asymmetric potential distribution, local potential barriers arising from the momentum imbalance of the excited plasmons, and an enhanced potential depth that permits stable trapping of nanoparticles using low-intensity laser beams. To investigate the performance of this platform, we develop a rigorous formalism based on Lorentz force within the Rayleigh approximation combined with anisotropic Green's functions and calculate the trapping potential of nonconservative lateral forces using the Helmholtz decomposition method. Tailored anisotropic and hyperbolic metasurfaces, commonly implemented by nanostructuring thin metallic layers, permit to use low-intensity laser sources operating in the visible or infrared frequencies to trap and manipulate particles at the nanoscale, and may enable a wide range of applications in bioengineering, physics, and chemistry.

I. INTRODUCTION

Optical trapping of small particles in the micrometer range has triggered numerous applications in microbiology [1–3], colloidal dynamics [4], and lab-on-a-chip applications [5], among many others [6–9]. In conventional optical tweezers [10–13], an optical trap is set through a tightly focused laser beam that confines the particle near the higher electric field intensity. There, the gradient of the electric field intensity that surrounds the particle generates the required trapping forces. Unfortunately, it is challenging to extend this approach to trap particles whose size lie down in the nanometer range as (i) the gradient force significantly lessens with the third power of the particle size [14]; and (ii) the thermal-fluctuation-induced motion of the particles increases [15,16], thus favoring them to escape from the trap. As a result, stable trapping demands high-intensity and tightly focused laser beams that may damage the nanoparticles due to photoheating.

These challenges can be alleviated by exploiting the properties of surface plasmon polaritons (SPPs) [17–20],

which are confined electromagnetic waves that propagate at dielectric-metal interfaces [21]. For instance, let us consider an electrically polarizable Rayleigh nanoparticle (with radius $a < \lambda_0/20$, where λ_0 is the wavelength) located near the surface of a metal is illuminated with light. The particle scatters the incoming light as a superposition of propagative plane waves and evanescent waves. This linear scattering process can be accurately modeled using the angular spectrum representation of a source considering that the particle behaves as a polarized electrical-point emitter [21]. When the particle is located in the near field of the plasmonic surface, the scattered evanescent waves can couple to the structure and excite guided SPPs [22–27]. Remarkably, this evanescent-wave coupling is governed by spin-orbit interactions [28–30]: only those surface plasmons that possess identical transverse spin to the one of the incoming waves will be excited. In the cases that the particle acquires a linear polarization, the scattered evanescent spectrum lacks any spin and excites SPPs propagating along all directions within the surface. The situation is different when the particle acquires an out-of-plane polarization spin with respect to the surface, which usually occurs when it is illuminated by an obliquely incident circularly polarized light [22]. There,

*jsgomez@ucdavis.edu

the scattered evanescent spectrum acquires a transverse spin and excites only SPPs with similar spin thus leading to plasmons traveling towards a specific direction along the surface. To compensate the momentum of these directional SPPs, a nonconservative recoil force is exerted on the particle acting in the direction opposite to the plasmons' wavevector [22–27]. The direction and strength of this force mostly depend on the handedness of the particle polarization spin and the momentum of the excited plasmons, respectively [23]. Aiming to boost the strength of recoil force, anisotropic and hyperbolic metasurfaces (HMTSs) have been proposed to substitute bulk plasmonic metals [31]. HMTSs [32–39] are ultrathin surfaces that exhibit a metallic or dielectric response as a function of the electric field polarization, possess a very large local density of states, and support ultraconfined SPPs over a broadband frequency range. These structures can be constructed by appropriately patterning common plasmonic materials, such as silver [38], gold [39], or graphene [34,35]. It has been shown that the recoil force acting on nanoparticles located over HMTSs can be enhanced up to several orders of magnitude with respect to the one appearing over bulk isotropic surfaces [31]. Such a giant enhancement is enabled by the large momentum of the directional hyperbolic plasmons excited during the scattering process. Furthermore, the enhancement is broadband [31] in the sense that it appears when the particle is illuminated with light oscillating at any frequency within a very wide range in which the structure exhibits a hyperbolic response. It should be noted that enhanced recoil force can also be obtained using bulk hyperbolic metamaterials [25]. However, the strength of such a force is weaker than the one found above hyperbolic metasurfaces and appears over a short wavelength span [31]. This is because the excitation of internally propagating hyperbolic states with sources located outside the bulk of the media is challenging, as evanescent fields scattered by the sources would mainly couple at the interface between the metamaterial and the surrounding environment [40].

In this context, recoil force has recently been exploited to trap nanoparticles near bulk metals using a linearly polarized Gaussian beam [41]. This elegant approach takes advantage of the peculiar distribution of the electric field within the beam: the components parallel to the surface are even symmetric with respect to the laser-beam axis whereas the out-of-plane component is odd symmetric. The interplay between even and odd symmetries of the in- and out-of- plane electric field components enforces that the nanoparticle acquires an out-of-plane polarization spin with a rotation handedness always pointing away from the beam axis that excites SPPs toward this direction. This response holds independently of the particle position within the beam. The combination of recoil force coming from the excitation of directional SPPs in the scattering process together with gradient force originating from the

Gaussian beam generates an optical trap located exactly at the beam axis [41]. Unfortunately, this platform might not be suitable for many practical applications because it requires specific laser sources operating at wavelengths very close to the intrinsic plasmon-resonance frequency of metals. As the laser operation frequency is shifted away from such a resonance, the presence of the metals does not play a significant role on the force acting on the particle and the trap performance becomes similar to a common optical tweezer governed by gradient force originating from the Gaussian beam. In addition, the performance of this approach in terms of potential distribution, trap depth, and minimum beam intensity required to achieve stable optical trapping has not yet been investigated. The calculation of these parameters is challenging due to the intrinsic nonconservative nature of the recoil force, which prevents the use of common theoretical approaches based on the definition of potential energy in the case of conservative force fields [21].

In this contribution, we propose stable optical trapping of nanoparticles using ultrathin anisotropic and hyperbolic metasurfaces illuminated with low-intensity Gaussian beams. This platform, illustrated in Fig. 1, permits to engineer optical traps in which recoil force coming from the directional excitation of ultraconfined SPPs determines the overall performance of the traps. The incident Gaussian beam enforces that the nanoparticle acquires an adequate out-of-plane polarization spin and sets the optical trap at its axis. Strikingly, and in stark contrast with the case of bulk metals studied in Ref. [41], the properties of the traps are directly linked with the anisotropic and broadband features of the supported SPPs, and can be modified by tailoring the electromagnetic response of the metasurface. In general, and compared to traps set over common isotropic surfaces (bulk metal and uniform thin layers), the proposed optical traps exhibit (i) *significantly larger trapping forces*, associated to the high momentum of the supported plasmons; and (ii) *a broadband response*, in the sense that stable trapping can be set with beams oscillating at any frequency within a wide range in which anisotropic metasurfaces support SPPs. To investigate this platform, explore its practical viability, and compare its performance with respect to other configurations, we develop below a rigorous theoretical formalism based on (i) the Lorentz force within the dipole approximation merged with anisotropic Green's functions [21] to compute the trapping forces; and (ii) the Helmholtz decomposition method [42] to compute the potential energy of nonconservative forces. We validate our results using full-wave numerical simulations performed in COMSOL Multiphysics [43]. Our approach permits calculation of the spatial potential distribution of the trap, including the trap depth, and allows elucidation of the minimum beam intensity required to achieve stable optical trapping. We apply our formulation to explore the trapping response of three realistic
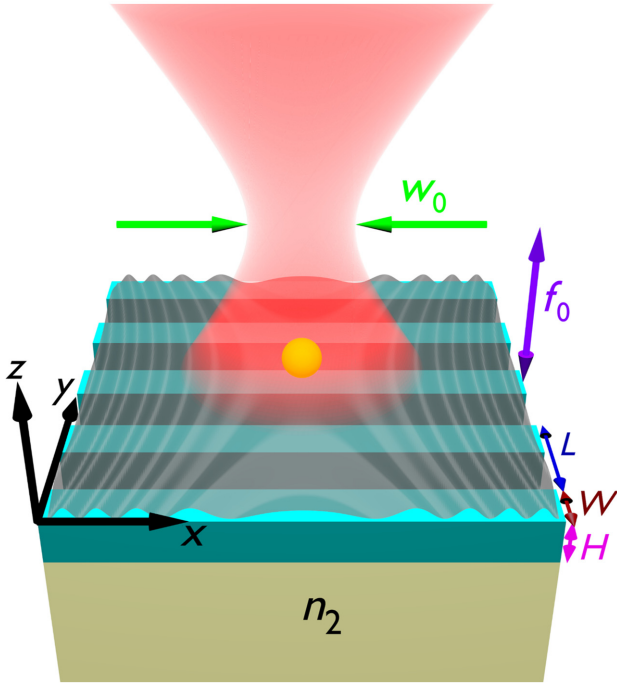
FIG. 1. Hyperbolic optical trap created by illuminating a Rayleigh particle (yellow) located above an ultrathin anisotropic metasurface (cyan) with a p-polarized Gaussian beam (red). The beam has width w_0 and is focused at a distance f_0 normal to the surface. During the light-scattering process, the particle excites highly confined surface plasmons (gray) on the metasurface propagating away from the beam axis where the optical trap is generated. The hyperbolic metasurface is constructed using subwavelength metallic rods with width W, height H, and periodicity L, and is supported by a medium of refractive index n_2.

configurations, namely a bulk silver substrate, a uniform and thin silver layer, and an array of densely packed silver nanostrips [38] that behaves as a HMTS. Numerical results reveal an outstanding trap performance of nanostructured silver over an ultrawide frequency band ranging from the visible to the infrared. Compared to the case of a thin silver layer or bulk silver, the nanostructured configuration greatly enhances the trap depth over the entire band that in turn reduces the beam intensity required to achieve stable optical trapping. It should be noted that at the plasmon resonance, the thin silver layer exhibits better performance than the other platform. This response appears because the nanostructured configuration does not exhibit a hyperbolic response at that wavelength. Then, we explore the asymmetrical potential distribution of the traps as the topology of the nanostructured silver layer evolves from elliptical to hyperbolic regimes going through its topological transition, and we reveal the presence of local potential barriers that might appear along precise directions within the surface. Such potential barriers arise over anisotropic surfaces thanks to its rotationally asymmetric response,

exhibit larger energy than the trap depth, and might be useful to predict the direction taken by an energetic particle to escape from the trap. This response is in stark contrast with the rotationally symmetrical and smooth potential distribution of traps set over thin and bulk metals, which are isotropic in nature. Anisotropic and hyperbolic metasurfaces are promising candidates to trap and manipulate nanoparticles using low-intensity laser sources operating in the visible and near-IR band, and might lead to useful applications in a wide variety of fields ranging from physics and chemistry to bioengineering.

II. THEORETICAL FORMALISM: TRAPPING FORCES AND POTENTIAL OVER ANISOTROPIC METASURFACES

This section details first a theoretical framework able to compute the nonconservative optical forces exerted on a dipolar Rayleigh particle located above an anisotropic metasurface that is illuminated by a Gaussian beam. Then, the spatial potential distribution of the trap is computed using the Helmholtz decomposition method [42]. Our formalism permits quantitative determination of relevant parameters such as the trap depth and stiffness, trapping forces and potential, and minimum beam intensity required to achieve stable trapping, among others. The approach is general in the sense that no assumptions have been made with respect to the type of metasurface, Rayleigh particle, surrounding media, and operation frequency.

A. Optical trapping forces over anisotropic metasurfaces

Let us consider an isotropic, nonmagnetic, and electrically polarizable spherical Rayleigh particle located at a position $\bar{r}_0 = (x_0, y_0, z_0)$ above an anisotropic metasurface defined by a conductivity tensor $\bar{\bar{\sigma}}^{\text{eff}} = \sigma_{xx}^{\text{eff}} \hat{x}\hat{x} + \sigma_{yy}^{\text{eff}} \hat{y}\hat{y}$, as shown in Fig. 1. The ultrathin metasurface is placed in the plane $z = 0$, lying on the interface between two media with refractive indices n_1 (top) and n_2 (bottom). The particle is illuminated by a normally incident Gaussian beam, i.e., the beam axis is aligned with the $\hat{z}$ axis (see the Supplemental Material [44]), that has a beam width w_0 and is focused at a distance f_0. The focus position f_0 is defined as the vertical distance between the metasurface and the center of the Gaussian beam (see the Supplemental Material [44]), and it is positive (negative) when the beam is focused above (below) the metasurface. Assuming an $e^{-i\omega t}$ time dependence, the total time-averaged optical forces exerted on the particle are given by [21]

$$\bar{F} = \frac{1}{2}\text{Re}\{\bar{p}^* \cdot \nabla[\bar{E}^{GW}(\bar{r}_0) + \bar{E}^s(\bar{r}_0)]\}. \quad (1)$$

Here, $\bar{p} = \alpha_0[\bar{E}^{GW}(\bar{r}_0) + \bar{E}^s(\bar{r}_0)] = \bar{\bar{\alpha}} \cdot \bar{E}^{GW}(\bar{r}_0)$ is the particle's electric dipole moment, α_0 is the dynamic

particle polarizability [21], $\bar{\bar{\alpha}}$ is the effective dipole polarizability tensor taking into account the electric field scattered by the particle that is reflected from the surface computed via the scattered dyadic Green's function [21,44], $\bar{E}^S$ is the electric field scattered by the particle, and $\bar{E}^{GW}$ is the superposition of the electric field of the standing wave formed due to the superposition of incident laser beam and its reflection from the metasurface. Equation (1) shows that the total forces acting on the nanoparticle are composed of two components: (i) the conservative gradient force, $\bar{F}_{\mathrm{grad}} = 0.5\,\mathrm{Re}[\bar{p}^* \cdot \nabla\bar{E}^{GW}(\bar{r}_0)]$, that always acts toward the higher electric field intensity of the standing wave [45,46]; and (ii) the nonconservative recoil force, $\bar{F}_{\mathrm{rec}} = 0.5\,\mathrm{Re}[\bar{p}^* \cdot \nabla\bar{E}^s(\bar{r}_0)]$ that appears to compensate the momentum of the directional SPPs excited on the surface [22–25,31]. These two force components have a very different origin: the gradient force depends on the gradient of the electric field intensity surrounding the particle, and thus varies with the type of beam employed. For instance, in the case of plane waves, this term would lead to a radiation pressure pointing toward the direction of

the wavefront; whereas in the case of a Gaussian beam, this component leads to gradient force pointing towards the beam center, as is common in optical tweezers [12]. On the other hand, the recoil force mostly depends on the properties of the surface plasmons supported by the metasurface [31]. Besides, this force also depends on the effective dipole polarization acquired by the particle [31]. For a given distance between the particle and the metasurface, the recoil force is maximized (strictly zero) when the particle acquires an out-of-plane (linear) polarization spin.

The electric field of the *p*-polarized (i.e., transverse magnetic) Gaussian beam employed in the proposed platform possesses x and y components (in plane) that are even symmetric with respect to the beam axis, whereas the z component (out of plane) is odd symmetric [41]. This field distribution ensures that the nanoparticle is polarized with a spin that rotates against the beam axis (see the Supplemental Material [44]), as shown in Fig. 2 (top inset). The resulting nonparaxial electric field components above the surface yield [21,47,48]

$$E_x^{GW}(\bar{r}) = \frac{w_0^2}{4\pi} \int\!\!\!\int\limits_{-k_1}^{k_1} \left[\frac{k_x k_{z1}}{k_t k_1} e^{-ik_{z1}z} - \left(R_{sp}\frac{k_y}{k_t} + R_{pp}\frac{k_x k_{z1}}{k_t k_1} \right) e^{ik_{z1}z} \right] e^{-\frac{k_t^2 w_0^2}{4}} e^{ik_{z1}f_0} e^{i(k_x x + k_y y)}\, dk_x dk_y, \tag{2a}$$

$$E_y^{GW}(\bar{r}) = \frac{w_0^2}{4\pi} \int\!\!\!\int\limits_{-k_1}^{k_1} \left[\frac{k_y k_{z1}}{k_t k_1} e^{-ik_{z1}z} - \left(R_{sp}\frac{k_x}{k_t} - R_{pp}\frac{k_y k_{z1}}{k_t k_1} \right) e^{ik_{z1}z} \right] e^{-\frac{k_t^2 w_0^2}{4}} e^{ik_{z1}f_0} e^{i(k_x x + k_y y)}\, dk_x dk_y, \tag{2b}$$

$$E_z^{GW}(\bar{r}) = \frac{w_0^2}{4\pi} \int\!\!\!\int\limits_{-k_1}^{k_1} \frac{k_t}{k_1} (e^{-ik_{z1}z} + R_{pp} e^{ik_{z1}z}) e^{-\frac{k_t^2 w_0^2}{4}} e^{ik_{z1}f_0} e^{i(k_x x + k_y y)}\, dk_x dk_y. \tag{2c}$$

Here, k_1 is the wave number in the medium above the surface with a transverse component $\bar{k}_t = \hat{x}k_x + \hat{y}k_y$ and a vertical component $k_{z1} = \sqrt{k_1^2 - k_t^2}$; and R_{pp} and R_{sp} are the Fresnel reflection coefficients that characterize the reflection of "*p*" and "*s*" polarized waves from the anisotropic surface when it is illuminated with "*p*"-polarized waves (see the Supplemental Material [44]). In addition, a phase shift $e^{ik_{z1}f_0}$ is introduced as a measure of tuning the laser focus position f_0 along the $\hat{z}$ axis [21,41]. Note that the integration limits in Eq. (2) are set to $\pm k_1$, because the propagative modes dominate the response of the beam and the influence of evanescent spectrum is

negligible [41]. In most scenarios, the total fields described in Eq. (2) keep a similar symmetry as the incident Gaussian beam in free space and polarize the particle with the desired handedness to enable optical trapping (see the Supplemental Material [44]). It should be noted that the symmetry of these fields may change when the Gaussian beam is focused well below the metasurface. In that case, described below, the particle may acquire an out-of-plane polarization spin with rotation handedness pointing toward the beam axis and the recoil force becomes an "antitrapping" force [41].

From Eq. (1), the lateral components of the gradient and recoil forces can be simplified as (see the Supplemental
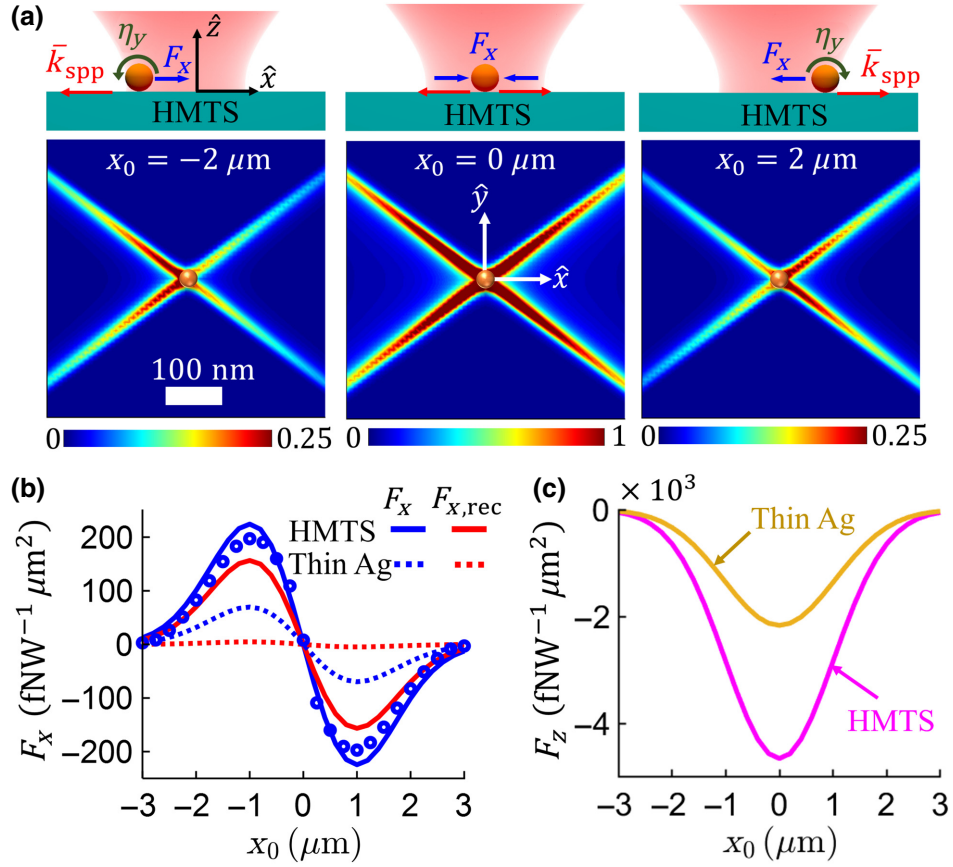
FIG. 2. Trapping Rayleigh particles over a nanostructured metasurface with a Gaussian beam. (a) Normalized power of the surface plasmons excited on the surface when the particle is located in different positions with respect to the beam axis. The top inset illustrates the dipole polarization spin that rotates against the beam axis, direction of the plasmon wavevector, and the recoil forces acting on the particle. (b) Total lateral forces F_x (blue solid line) and recoil forces $F_{x,\text{rec}}$ (red solid line) exerted on the nanoparticle versus its position with respect to the beam axis (see the Supplemental Material [44]). Results obtained above actual nanostructured silver using COMSOL Multiphysics (markers) are included for validation [43]. Dotted lines correspond to the forces acting on the nanoparticle when the metasurface is replaced by a thin silver layer of identical thickness as the nanostructured metasurface. (c) Attractive vertical forces F_z acting on the nanoparticle as a function of its position x_0 with respect to the beam axis. The gold nanoparticle has a radius $a = 15$ nm and is located in free space at a distance $z_0 = a$ over the metasurface described in Fig. 1 with parameters $W = 60$ nm, $L = 180$ nm, $H = 10$ nm, and $n_2 = 1.05$. The Gaussian beam width is $w_0 = 2\,\mu$m, focus is $f_0 = 0$, and its operating wavelength is 540 nm.

Material [44])

$$\bar{F}_{\text{lateral,grad}} = \frac{1}{2} Re \sum_{n=x,y,z} \left[p_n^* \frac{d}{dx} E_n^{GW}(\bar{r}_0)\hat{x} + p_n^* \frac{d}{dy} E_n^{GW}(\bar{r}_0)\hat{y} \right],$$

(3a)

$$\bar{F}_{\text{lateral,rec}} = -\omega^2 \mu_0 \left\{ \text{Im}[p_x^* p_z]\text{Im}\left[\frac{d}{dx} G_{xz}^s(\bar{r}_0) \right]\hat{x} \right.$$

$$\left. + \text{Im}[p_y^* p_z]\text{Im}\left[\frac{d}{dy} G_{yz}^s(\bar{r}_0) \right]\hat{y} \right\}.$$

(3b)

Equation (3a) shows that the gradient force always acts toward the maximum electric field intensity (i.e., toward the beam axis) of the standing wave formed above the metasurface. In addition to the type of beam, this force

also depends on the particle's polarizability [21]. Equation (3b) shows that the direction of the recoil force is determined by the interplay between the particle's in-plane (p_x and p_y) and out-of-plane (p_z) dipole-moment components. Using a properly focused Gaussian beam, the particle acquires an out-of-plane polarization spin with rotation handedness against the beam axis and the resultant recoil force is directed towards the beam axis. In the case of isotropic metasurfaces, this force points exactly towards the beam axis independently of the particle position within the beam [41]. However, in the case of anisotropic metasurfaces, the direction of the recoil force may not point towards the beam axis due to the broken rotational symmetry of the system [i.e., $G_{xz}^s(\bar{r}_0) \neq G_{yz}^s(\bar{r}_0)$ in Eq. (3b)]. As discussed below, the recoil force then pushes the particle towards the beam axis following a parabolic trajectory. In addition, Eq. (3b) unveils that the strength of the recoil

force depends on the imaginary part of the spatial derivative of scattered Green's functions' out-of-plane tensor component, which measures the momentum of the excited directional plasmons [23,31].

A useful parameter that defines the performance of an optical trap is the trap stiffness, which measures the restoring force that acts on the nanoparticle to bring it back to a stable position within the trap—similar to the spring constant in a common mechanical system. This parameter is more significant in Brownian systems, where particles suspended in liquids may acquire random motion due to the continuous collision with the moving fluid molecules. The stiffness of a trap set over a surface can be approximated as [49]

$$\kappa(\phi) = -\frac{F_\rho(\rho, \phi)}{\rho}\bigg|_{\rho \to 0}, \tag{4}$$

where $F_\rho(\rho, \phi)$ denotes the radial component of the lateral forces evaluated at a position (ρ, ϕ) defined in polar coordinate system. In Eq. (4), we assume that the tangential force component is significantly weaker than the radial one, as happens in the plasmonic systems considered here (see the Supplemental Material [44]). In most cases considered in the literature [12,41], for instance, the force generated by Gaussian beam in free space or over common plasmonic materials, the trap stiffness is isotropic in the sense that it has polar symmetry and therefore provides an identical response in all directions: $\kappa(\phi) = \kappa$. This is different in the case of traps set over anisotropic metasurfaces: the restoring force that a nanoparticle experiences towards the trap depends on the direction through which the particle is trying to escape. Traps with anisotropic stiffness are useful to predict the probable direction followed by the particle when it acquires enough energy to escape from the trap.

B. Trapping potential over anisotropic metasurfaces

The trap potential is arguably the most useful parameter that defines the performance of an optical trap [17,18,50]. Here, we focus on the trap potential energy and trap depth, which is a quantitative measure of how long the particle remains confined within the trap. In the case of conservative forces, such as the gradient force originating from a Gaussian beam [13], the trapping potential U of a vector force $\bar{F}_c$ can be obtained as $U_c(\bar{r}) = -\int_{-\infty}^{\bar{r}} \bar{F}_c(\bar{r}') \cdot d\bar{r}'$ [21]. This potential represents the energy required to move a particle from a reference location with zero energy (considered here to be in the infinite) to the position defined by the vector $\bar{r}$. Conservative forces are free of solenoidal components and thus the path chosen in the integral is not relevant: any trajectory from infinite to $\bar{r}$ provides identical potential energy. This situation is different in the case

of nonconservative vector forces because they possess a solenoidal component [51]. Nonconservative forces may arise in many scenarios, for instance, in certain optomechanical systems [52], using structured or evanescent fields [53], or when a nanoparticle is illuminated near a plasmonic surface [22–26,31]. In such cases, choosing different paths to move the particle from a reference location to a position $\bar{r}$ will lead to different potential energies due to the presence of the solenoidal force component. As a result, it is not possible to use direct integration methods to compute the potential energy. To avoid this issue, we apply here the Helmholtz decomposition method to compute the trapping potential of nonconservative forces [42]. Following this approach, we express the force field as [51–53]

$$\bar{F}(\bar{r}) = -\nabla U + \nabla \times \bar{A}, \tag{5}$$

where ∇ is the vector gradient, U is the potential energy, $\bar{A}$ is the vector potential, and ∇U and $\nabla \times \bar{A}$ denote the conservative and nonconservative (solenoidal) force components, respectively. Taking the divergence of Eq. (5) and applying the identity $\nabla \cdot (\nabla \times \bar{A}) = 0$ permit us to find the potential energy through the differential equation [51]

$$-\nabla^2 U = \nabla \cdot \bar{F} \text{ on } \Omega,$$

which is subjected to the Neumann boundary conditions [54]

$$\nabla U \cdot \hat{\rho} = \bar{F} \cdot \hat{\rho} \text{ on } d\Omega,$$

where $\hat{\rho}$ is a unit vector pointing outwards with respect to the boundary of the domain Ω. This numerical approach is valid when the force field is defined over a bounded region Ω with a smooth boundary condition $d\Omega$. We stress that the platform considered here fulfils these conditions: the domain is defined by the Gaussian beam impinging over the metasurface and the boundary conditions are related to the negligible force acting on the particle when it is located very far away from the beam axis.

We explore the potential distribution of the optical-trap set using Gaussian beams over isotropic surfaces, for instance ultrathin and bulk metals, and reveal that they are defined by a spatially rotational symmetric function centered at the beam axis. In stark contrast, the trapping potential over anisotropic metasurfaces illuminated with a Gaussian beam lacks such a rotational polar symmetry. In both cases, the trap depth δ_d is unique and is defined as the potential difference between the energy computed at the beam axis and at a position located in infinite with zero energy. Strikingly, and as further detailed below, the intrinsic anisotropy of the metasurface gives rise to *local potential barriers* with larger potential difference than the trap depth. As a result, the particle might acquire enough energy to escape from the trap but not to overcome such potential barriers and thus will follow a special route

within the plane to avoid them. Finally, it should be noted that stable optical trapping appears when the trap depth is larger than $10k_BT$, where k_B is the Boltzmann constant and T is temperature. If this condition is not fulfilled, mechanisms such as thermal fluctuation [55,56] and Brownian motion [12,17,53] may provide enough energy to the particle to quickly escape from the trap. Thus, the minimum laser-beam intensity required to achieve stable trapping is the one required to generate an optical trap with a potential depth $\geq 10k_BT$ [21].

III. PERFORMANCE OF OPTICAL TRAPS ENGINEERED OVER ANISOTROPIC AND HYPERBOLIC METASURFACES

In this section, we explore the performance of optical traps engineered over anisotropic and hyperbolic metasurfaces illuminated by a p-polarized Gaussian beam. To this purpose, we first analyze the recoil and gradient forces acting on a nanoparticle versus its position with respect to the beam axis, unveiling the mechanisms that conform the optical trap. Then, we investigate key parameters of the trap including trap depth and stiffness, spatial potential distribution, local potential barriers, and the laser-beam intensity needed to achieve stable trapping versus the wavelength of the incoming beam. As the wavelength increases, the metasurface topology evolves from an anisotropic elliptical to a hyperbolic regime going through a topological transition, which permits the study of how the different light-matter interactions enabled by these regimes conform the properties of the optical trap. During our study, we compare the performance of the proposed traps to the one found using Gaussian beams in free space [11,12], bulk metals [41], and thin films, aiming to highlight the pros and cons of this platform with respect to other configurations and to assess its practical viability.

In the following, we consider a spherical gold nanoparticle of radius $a = 15$ nm located at $\bar{r}_0 = (x_0, y_0, a)$. The metasurface is constructed using nanostructured and periodic silver rods [38,57] with width $W = 60$ nm, height $H = 10$ nm, and periodicity $L = 180$ nm (see Fig. 1) patterned over a porous polymer with refractive index $n_2 = 1.05$ [25]. The subwavelength thickness and periodicity of the layer allow us to characterize it using an effective in-plane conductivity tensor [58–61] with negligible out-of-plane polarizability [62,63]. Even though the use of different substrates might change the particle polarizability and the density of states provided by the structure, the overall response will not be significantly affected (see the Supplemental Material [44]). We carefully verify the accuracy of our model using full-wave numerical simulations as well as the dispersive hyperbolic response of the surface (see the Supplemental Material [44]). For comparison purposes, we employ ultrathin and bulk silver with identical

properties as the one employed on the nanostructured metasurface (see the Supplemental Material [44]).

A. Optical forces arising in anisotropic traps

Figure 2 illustrates the response of the proposed optical trap detailing the different forces that act on the nanoparticle when it is illuminated with a Gaussian beam at 540 nm. At this wavelength, the nanostructured silver layer behaves as a hyperbolic metasurface (see the Supplemental Material [44]). For the sake of simplicity, we begin considering that the nanoparticle is located along the metallic rods (i.e., the $\hat{x}$ axis). In this situation, the polarization state acquired by the particle can be computed from dipole moment $\bar{p}(x_0) = [p_{xr}(|x_0|) + ip_{xi}(|x_0|)]\hat{x} + [\mp p_{zr}(|x_0|) \mp ip_{zi}(|x_0|)]\hat{z}$, where the subscripts "$r$" and "$i$" denote the real and imaginary components of a complex number, and the upper (lower) sign appears when the particle is located in the negative (positive) portion of the $\hat{x}$ axis (see the Supplemental Material [44]). We stress the symmetry of the electric dipole magnitude with respect to the beam axis, i.e., $|\bar{p}(x_0)| = |\bar{p}(-x_0)|$. This dipole can be expressed as a linear combination of two fundamental emitters that have opposite out-of-plane polarization rotation handedness with respect to the surface. The dipole moment of these emitters are $\bar{p}_1(x_0) = p_{xr}(|x_0|)\hat{x} \mp ip_{zi}(|x_0|)\hat{z}$ and $\bar{p}_2(x_0) = ip_{xi}(|x_0|)\hat{x} \mp p_{zr}(|x_0|)\hat{z}$. The excitation of $\bar{p}_1(\bar{p}_2)$ depends on the real (imaginary) and imaginary (real) parts of the in-plane and out-of-plane electric field components of the standing wave created over the surface. Focusing the incident p-polarized Gaussian beam close to the metasurface ensures that the real part of the in-plane electric field components is much stronger than the other ones (see the Supplemental Material [44]). As a result, the dipole $\bar{p}_1$ is strongly excited and dominates the scattering processes, generating SPPs that propagate in the radial direction against the beam axis. Figure 2(a) shows the power of the SPPs launched on the metasurface for several particle positions. When the particle is located away from the beam axis (i.e., $x_0 \neq 0$), it mostly scatters evanescent waves with a transverse spin that excites directional plasmons with wavevectors pointing away from the beam axis, associated with a "trapping" recoil force acting toward the beam axis. When the particle is located exactly on the axis of the Gaussian beam, it acquires a linear polarization $\bar{p}(x_0 = 0) = p_x(x_0 = 0)\hat{x}$ and scatters waves without any specific spin that excites SPPs propagating symmetrically through the surface. As a result, the recoil force vanishes, and an optical trap is set at $x_0 = 0$. It is worthwhile to note the role of the dipole $\bar{p}_2(x_0)$: it excites directional plasmons propagating towards the beam axis that result into "antitrapping" recoil force [41,44]. In the case shown in Fig. 2, the magnitude of this emitter is very small (see the Supplemental Material [44]) and thus it barely contributes to the excitation of SPPs. In a more

general case, it is possible to engineer trapping or anti-trapping recoil forces by controlling the strength of the orthogonal dipoles that characterize the electromagnetic response of the particle. This can be done by manipulating the properties (focusing, polarization, etc.) of the incident Gaussian beam.

The total optical forces exerted on the nanoparticle are determined by the superposition of gradient and recoil forces. Figure 2(b) shows the x component of the total (blue solid line) and recoil (red solid line) forces versus the particle position along the $\hat{x}$ axis. For the sake of comparison, it also shows these forces arising when the nanostructured layer is replaced by a thin silver layer (dashed lines) of similar thickness. Results show that the recoil force strength over nanostructured silver is more than an order of magnitude (approximately 40 times) larger than the one found over the thin layer. This enhancement appears thanks to the large wave number (momentum) of the surface plasmons excited over the nanostructured surface. As a result, the trapping mechanism is very different in both platforms: above the thin silver layer, the trap is dominated by the gradient force generated from the Gaussian beam and its reflection from the surface; above the nanostructured silver layer, the trap is primarily determined by the strong recoil force originating from the directional excitation of hyperbolic surface plasmons. Overall, the hyperbolic response of nanostructured silver enhances the total lateral force strength over 6 times with respect to the nonpatterned case. This example highlights how anisotropic metasurfaces can enable plasmon-assisted optical traps at desired wavelengths determined by the surface properties. Figure 2(c) compares the vertical forces acting on the particle when it is located over these two configurations. In both cases, the total vertical force is dominated by the recoil force, which is always attractive, pushes the particle towards the surface, and exhibits a maximum strength near the trapping position. Note that

a nanoparticle located above a bulk silver substrate experiences a repulsive vertical force due to the dominant contribution of the gradient component, whereas the lateral components exhibit a similar response as in the case of thin silver (see the Supplemental Material [44]).

Numerical full-wave simulations performed in COMSOL Multiphysics (markers) are included in Fig. 2(b). Results are obtained considering realistic nanostructured silver and applying Maxwell's stress tensor formalism as described within the Supplemental Material [44]. Our study shows that the effective medium approach can be applied to model the trap response of hyperbolic structures even though the particle is in the near field. It should be noted that small ripples appear on the force exerted on the particle as it moves along the $\hat{y}$ axis from one metallic rod to another one through the airgap in between them (see the Supplemental Material [44]). These ripples are associated to near-field interactions not captured by homogeneous models and become stronger as the operation wavelength decreases and the particle is electrically closer to the surface. We verify that these ripples have a limited impact on the force amplitude and its spatial profile, and therefore they do not change the performance of the proposed optical traps.

Although our study above is focused on nanoparticles located along the metallic rods of the nanostructure ($\hat{x}$ axis in the coordinate system of Fig. 1), the underlying mechanisms hold independently of the particle position within the surface (see the Supplemental Material [44]). Figure 3 explores this scenario and shows the components of the lateral forces acting on the particle as well as a quiver plot indicating the force direction. Results confirm that an optical trap is created exactly at the beam axis. Furthermore, this analysis reveals the intrinsic anisotropy of the metasurface: the strength of the recoil force exerted on the nanoparticle lacks rotational symmetry. This asymmetry appears because SPPs traveling towards different
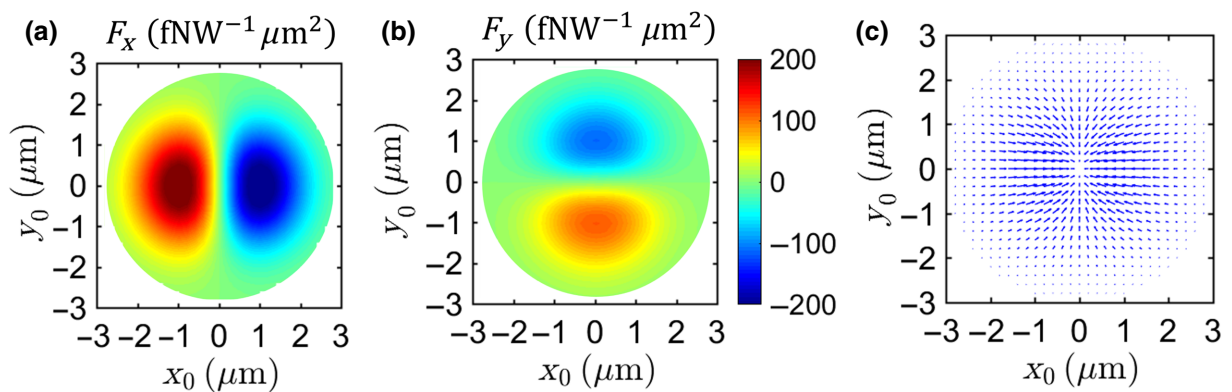

FIG. 3.   Optical trapping of a Rayleigh particle located above a hyperbolic metasurface when it is illuminated with a Gaussian beam. (a), (b) Lateral components of the total force acting on the nanoparticle versus its position (x_0, y_0) with respect to the beam axis. (c) Quiver plot detailing the direction of the lateral forces. Other parameters are as in Fig. 2.

directions within the surface possess different momentum and spin, and the resulting force might not be directly directed towards the beam center. Instead, the particle follows a parabolic trajectory towards the trap, as shown in Fig. 3(c). Note that the recoil force is significantly larger than gradient force for all particle positions and thus determines the trap performance.

B. Performance of anisotropic optical traps versus wavelength

Figure 4(a) shows the potential depth of the traps engineered over nanostructured silver versus the wavelength of the incident Gaussian beam. Results are normalized with respect to the beam intensity available at the focus position. This figure highlights *the extreme bandwidth in which*
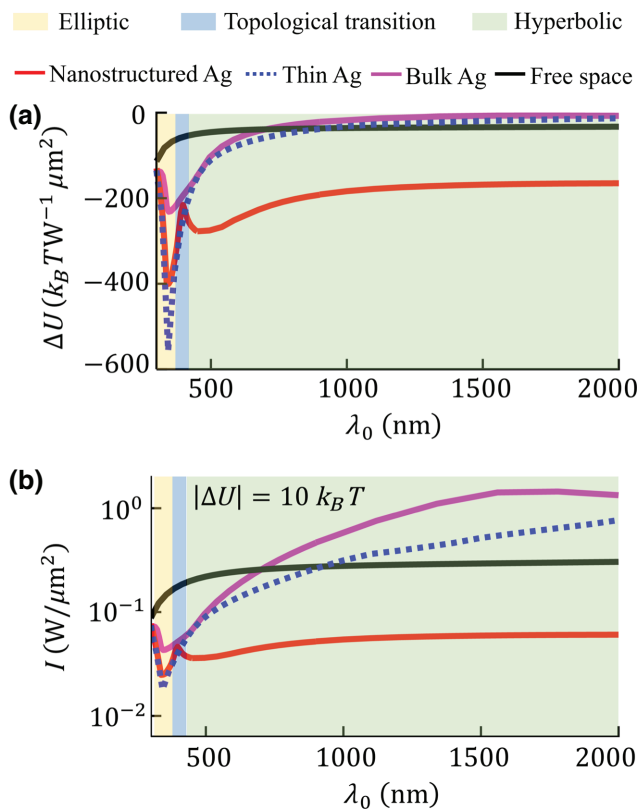

(a)

(b)

FIG. 4. Performance of optical traps engineered over anisotropic metasurfaces versus frequency. (a) Trap depth normalized with respect to the power density available at the center of the incident Gaussian beam. (b) Minimum amount of power density required to achieve stable trapping. Results are computed for a nanoparticle that is illuminated by a Gaussian beam and is located above an array of silver nanorods (red), above bulk silver (magenta), above a thin silver layer (dotted blue), and in free space (black). The background shaded region corresponds to different metasurface topologies (yellow, elliptic; green, hyperbolic) going through the topological transition (blue) associated with the nanostructured silver layer. Other parameters are as in Fig. 2.

optical traps with very large potentials can be set, covering the band from around 300 nm to over 2 μm, and how the trap depth correlates to the metasurface topology. Theoretically, the structure exhibits hyperbolic responses in the near-IR and beyond. However, due to the difficulty to appropriately focus the beam at these frequencies and the smaller amount of power scattered by the particle there, we restrict our analysis to the visible portion of the spectrum. It should be noted that different types of anisotropic and hyperbolic metasurfaces can be designed to operate in the infrared region [64–67]. Figure 4(a) also shows the trap depth obtained with a similar Gaussian beam focused over a thin silver layer (blue dotted line), bulk silver (magenta solid line), and in free space in the absence of any structure (black solid line). Results show that a thin layer of silver enables optical trapping with a performance comparable to the nanostructured one in the range of 325–425-nm wavelength, and exhibits a slightly better trap depth (approximately 1.4 times) at the intrinsic plasmon-resonance frequency of silver (approximately 340 nm). This response appears for two main reasons. First, the proposed nanostructured silver behaves as a HMTS only for wavelengths larger than 425 nm. In the range of 340–425 nm, it behaves as an anisotropic elliptical surface (see the Supplemental Material [44]) that exhibits moderate density of states. Therefore, in this frequency range the comparison is between two elliptical surfaces, one isotropic and another anisotropic. We note that nanostructured silver can be redesigned to exhibit hyperbolic response in this frequency range (340–425 nm), but this might be challenging to fabricate in practice. Second, the electrical distance between the dipole and the surface is not negligible at 340 nm. There is a clear trade-off [22,23,31] between the particle-surface distance and the surface modes that can be excited: when the particle is located in the very near field of the surface, it can couple to surface plasmons with large wave numbers that boost the overall performance of the optical trap; when the particle is moved away from the surface, scattered fields are partially filtered out by free space and cannot efficiently excite surface plasmons. In the latter case, evanescent fields with low and moderate wave numbers are not strongly attenuated and can still couple to structures that support them, as happens in the case of a thin layer of silver. The combination of these two factors explains why a thin layer of silver exhibits a better response over nanostructured silver at 340 nm. In the case of bulk silver, maximum potential depth is obtained near 340 nm and is approximately 2 times weaker than the one obtained above nanostructured silver. When the particle is illuminated in free space in the absence of any configurations, the trap depth increases as the laser wavelength decreases, a response associated to the higher amount of power scattered by an electrically larger particle. Our results confirm that nanostructured silver exhibits very large trap depth over a very wide

bandwidth, which is not possible to achieve with uniform thin films. Figure 4(b) shows the minimum laser intensity required to achieve stable trapping (i.e., a trap depth approximately $10k_BT$) in these configurations. This study reveals that the nanostructured metasurface permits reduction of the required beam intensity by an order of magnitude with respect to the other platforms. This has significant implications in practice as it allows the use of low-intensity laser sources operating in the visible and IR region to trap and manipulate nanoparticles while avoiding delicate adjustment between the surface response and the laser wavelength.

To further investigate the performance of these platforms, Fig. 5 shows their isofrequency contours—i.e., slices of the two-dimensional (2D) momentum space (k_x, k_y) at a constant wavelength. These contours describe the wave number of the supported SPPs versus their direction in space and are very useful to engineer plasmonic optical traps. From the figure, it is evident that HMTSs support surface plasmons with larger momentum over a large wavelength range; whereas isotropic materials support surface plasmons with moderate momentum near the plasmon-resonance frequency of the material. The potential distribution of the traps above these structures are shown in Figs. 6 and 7. The potential energy is computed varying the particle position (x_0, y_0) over the surface with respect to the beam axis. At the silver plasmon resonance, found at $\lambda_0 \approx 340$ nm [44,57], both bulk and thin-film configuration support TM isotropic surface plasmons [Fig. 5(b)] that lead to a rotationally symmetric potential distribution around the beam axis [Figs. 6(b) and 6(c)]. At this frequency, the nanostructured silver layer behaves as an elliptical anisotropic surface [Fig. 5(a)] and supports rotationally nonsymmetric surface plasmons. Interestingly, the intrinsic metasurface anisotropy translates into a nonsymmetric potential distribution that is illustrated in a three-dimensional fashion in Fig. 6(a). Figure 7 further studies the one-dimensional potential distribution above this configuration when the particle is moved along the main axes (i.e., $\hat{x}$ and $\hat{y}$) of the metasurface. At 340-nm wavelength, along the silver nanorods (i.e., $\hat{x}$ axis with

$y_0 = 0$), the potential is spatially smooth, and the trap depth ($\nabla U_x = \delta_d$) corresponds to the difference between the potential energies when the particle is located at the beam axis and infinity. Across the strips (i.e., $\hat{y}$ axis with $x_0 = 0$), the potential presents local maxima with energy larger than zero that leads to local barriers with potentials greater than the trap depth ($\nabla U_y > \delta_d$). Such local potential barriers appear above anisotropic surfaces because they support surface plasmons with different wave numbers (momentum) along different polar directions within the surface. As a result, the lateral recoil force exerted on the particle strongly depends on its azimuthal position with respect to the beam axis. Remarkably, barriers with potential energies even larger than the trap depth can be obtained by leveraging extreme anisotropic responses, associated with SPPs possessing drastically dissimilar wave numbers as they travel towards different directions within the plane. This case can be found at the metasurface topological transition, which appears at $\lambda_0 = 390$ nm (see the Supplemental Material [44]) and exhibits a canalization-like response along the $\hat{y}$ direction [68]. There, plasmons propagating towards the $\hat{x}$ axis possess significantly larger momentum than those traveling toward the canalized direction, enabling local potential barriers along the strips [see Fig. 7(b)] with an energy $\nabla U_x > \nabla U_y = \delta_d$. In such a configuration, a trapped particle that gains kinetic energy will probably escape in the direction perpendicular to the nanorods, which in addition to lower potential also exhibits a reduced trap stiffness. It should be noted that the trap depth at this wavelength slightly decreases [Fig. 4(a)] due to the overall moderate local density of states exhibited by the metasurface [Fig. 5(a)]. However, the trap depth is still larger than the one found over uniform silver [Fig. 6(b)] because this material provide reduced light-matter interactions when operated off resonance. As the operation wavelength further increases, the nanostructured silver layer behaves as a hyperbolic metasurface and supports highly confined SPPs. Isofrequency contours of these SPPs and associated trapping potentials at $\lambda_0 = 540$ nm and $\lambda_0 = 785$ nm are shown in Figs. 5–7. Hyperbolic surfaces lead to asymmetric potential distribution and very
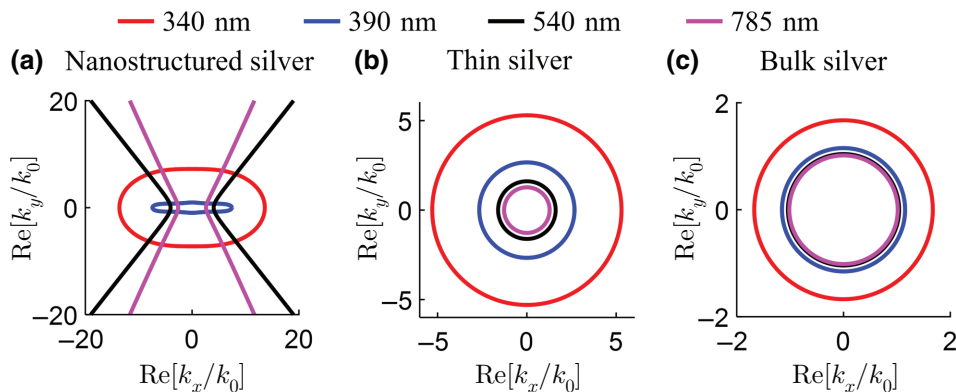

FIG. 5. Isofrequency contour of (a) a nanostructured silver layer; (b) a thin silver layer; and (c) bulk silver at different wavelengths. The physical dimensions of the nanostructure are detailed in Fig. 2.
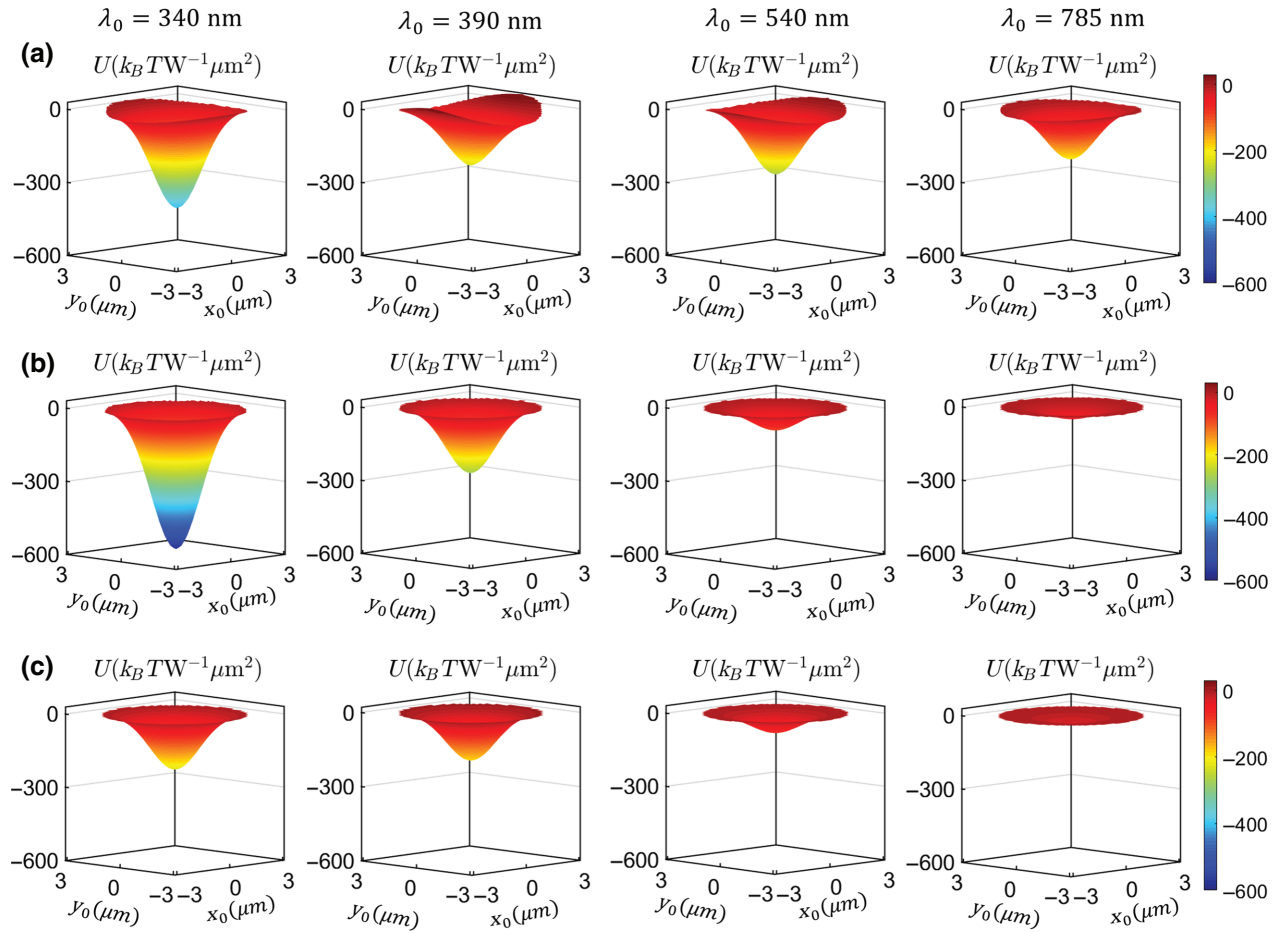
FIG. 6.   Trap potential versus the position (x_0, y_0) of the particle when it is illuminated by a Gaussian beam oscillating at 340-, 390-, 540-, and 785-nm operation wavelength. Results are computed when the particle is located above (a) a nanostructured silver layer; (b) a thin silver layer; and (c) bulk silver. Other parameters are as in Fig. 2.

significant trap depths, greatly extending the functionality of the proposed anisotropic platform from the visible toward the IR. Local potential barriers also arise in the hyperbolic case due to the different features of plasmons propagating towards x [see Fig. 2(a)] and y semiplanes. SPPs' properties evolve as the wavelength increases and the metasurface hyperbolic branches slowly close and tend to behave as in a canalization regime along the $\hat{x}$ direction, which in turn leads to local potential barriers across the nanorods (i.e., $\hat{y}$ axis). For comparison, thin-layer and bulk configuration mostly behave as a lossy dielectric reflector as the wavelength increases even further. At these frequencies, they do not effectively contribute to conform an optical trap rather than enhancing or decreasing the gradient force acting on the particle by modifying the standing-wave field patterns.

To complete our study, Fig. 8 shows the stiffness of the optical traps engineered over the considered platforms versus the beam wavelength and the azimuthal angle ϕ within the surface defined with respect to the positive $\hat{x}$

axis, i.e., along the strips. In the case of the nanostructured silver layer, the trap stiffness dramatically increases when the metasurface topology changes from elliptical TE to anisotropic elliptical TM, at around 340 nm. As happens with the potential, the stiffness exhibits a rotationally nonsymmetric distribution and, starting from the topological transition at 390 nm to around 750 nm, it presents local maxima in the directions along the metallic rods (i.e., $\phi = 0°$ and 180°) and minima in the orthogonal ones (i.e., $\phi = 90°$ and 270°). Such a response is associated to the distribution of the nonconservative force that conforms the trap [as the one shown in Figs. 3(a) and 3(b)] and consistent with the local potential barriers found along the strips shown in Fig. 7. Thus, it is probable that energetic particles will escape from these optical traps in the direction across the strips. As wavelength increases further, the metasurface changes its polarization profile and tends to canalize waves along the $\hat{x}$ axis. This mechanism swaps the direction of maximum (minimum) stiffness, which now appears across (along) the strips. In those optical traps, energetic
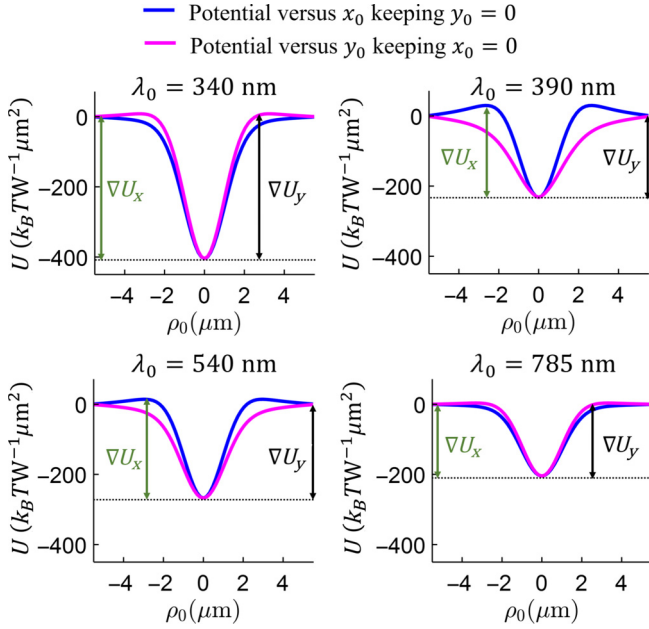
FIG. 7. Trapping potential computed as a function of the particle position (x_0, y_0) along (x_0 with $y_0 = 0$; blue line) and across (y_0 with $x_0 = 0$; magenta line) the nanorods of a nanostructured silver layer for several operation wavelengths. Local potential barriers along and across the nanorods are denoted as ΔU_x and ΔU_y, respectively. Other parameters are as in Fig. 2.

particles will escape in the direction parallel to the strips. For comparison, the trap stiffness obtained focusing the beam over a thin silver layer and over bulk silver is shown in Figs. 8(b) and 8(c). As expected, optical traps engineered over them show only better stiffness around the metal plasmon resonance and always exhibit a rotationally symmetrical profile around the trap. Overall, anisotropic metasurfaces significantly boost the stiffness of engineered optical traps over a large frequency band.

IV. CONCLUSIONS

We put forward the concept of anisotropic and hyperbolic optical traps to manipulate nanoparticles. These optical traps are created by illuminating a nanoparticle over an anisotropic metasurface with a linearly polarized Gaussian beam and their properties strongly depend on the surface topology and light-matter interactions. To analyze this platform, we develop a rigorous theoretical formalism able to compute the induced trapping forces based on the anisotropic scattered dyadic Green's function approach merged with the Lorentz force within the Rayleigh approximation. This approach, validated with full-wave numerical simulations in COMSOL Multiphysics, reveals that giant, nonconservative recoil force pointing towards the beam axis dominates the overall trap response. This force appears due to the excitation of ultraconfined SPPs on the anisotropic metasurface. Then, we apply the Helmholtz decomposition method to calculate the potential energy of the resulting nonconservative force field. Our formalism permits computation of fundamental metrics that characterize optical traps engineered over plasmonic materials through nonconservative fields, including spatial potential distribution, trap depth and stiffness, local potential barriers, as well as the minimum laser intensity that achieve stable optical trapping.

The performance of the proposed anisotropic optical traps is outstanding: they exhibit large trap depths over an extremely broadband frequency range that covers the entire visible spectrum extending well into the IR band. As a result, a wide variety of low-intensity laser sources can be employed to achieve stable trapping of nanoparticles avoiding precise alignments between the surface response and the operation wavelength, and significantly reducing the possibility of damaging trapped particles due to photoheating. As a specific example, we study the performance of optical traps engineered over a nanostructured silver layer and analyze how the trap response evolves as the
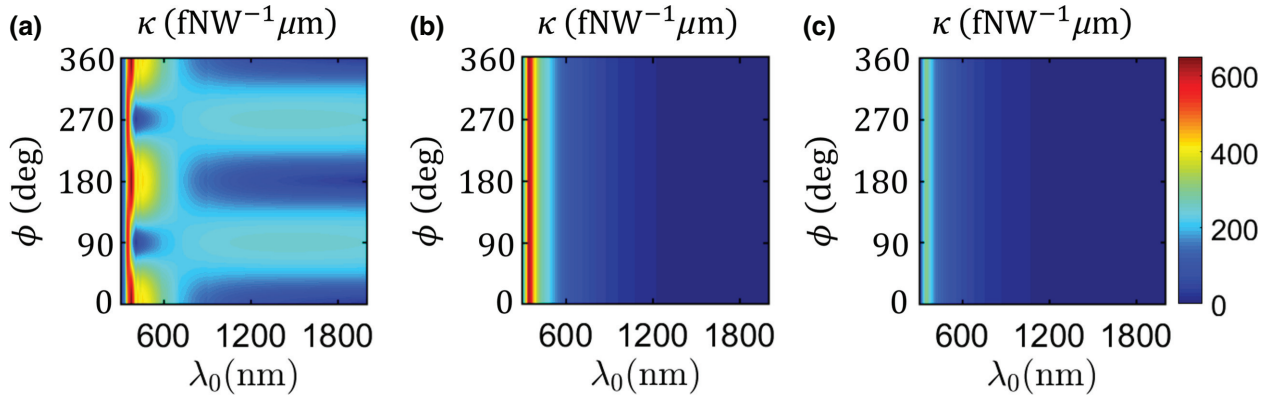

FIG. 8. Trap stiffness induced on a nanoparticle as a function of the wavelength (λ_0) of the incident Gaussian beam and the polar angle (ϕ) defined with respect to the $\hat{x}$ axis in Fig. 1. Results are computed for a nanoparticle that is illuminated by a Gaussian beam and is located above (a) a nanostructured silver layer; (b) a thin silver layer; and (c) bulk silver. Other parameters are as in Fig. 2.

metasurface topology changes from anisotropic elliptical to hyperbolic going through the topological transition. In addition, we find that the momentum imbalance of the SPPs excited by the particle on anisotropic surfaces gives rise to local potential barriers and larger trap stiffness along certain spatial directions, thus breaking the rotational symmetry that characterizes common optical traps. The engineered traps exhibit a much larger potential depth and stiffness than the one found focusing identical Gaussian beam over uniform thin silver, bulk silver or in free space, and maintain such a response over a large bandwidth. We note that our formalism is based on the semiclassical Maxwellian approach and omits additional forces that might originate from other mechanisms, such as Casimir forces [21,69]. Investigating the influence of such forces in the proposed platform is the scope of future research.

Moving forward, ultrathin metasurfaces enable unique possibilities to construct optical traps with excellent performance, including the possibility to engineer local potential barriers, at a desired wavelength, by tailoring the surface topology, local density of states, and the momentum of the supported plasmons. To this purpose, different plasmonic materials—including metals such as gold or silver and semimetals such as graphene and WTe_2 [70]—can be appropriately patterned in subwavelength arrangements. In addition, natural anisotropic and hyperbolic materials [71,72] can also be employed to trapping purposes, including hexagonal boron nitride [73], hybrid composites [74,75], van der Waals crystals [37,76–78], and an increasing family of 2D materials [64–67]. We envision that anisotropic and hyperbolic metasurfaces will lead to the next generation of low-power nano-optical tweezers.

ACKNOWLEDGEMENTS

---

[1] Y. Pang and R. Gordon, Optical trapping of a single protein, Nano Lett. **12**, 402 (2011).

[2] A. Ashkin and J. M. Dziedzic, Optical trapping and manipulation of viruses and bacteria, Science **235**, 1517 (1987).

[3] A. H. Yang, S. D. Moore, B. S. Schmidt, M. Klug, M. Lipson, and D. Erickson, Optical manipulation of nanoparticles and biomolecules in sub-wavelength slot waveguides, Nature **457**, 71 (2009).

[4] Y. Roichman, B. Sun, A. Stolarski, and D. G. Grier, Influence of Nonconservative Optical Forces on the Dynamics of Optically Trapped Colloidal Spheres: The Fountain of Probability, Phys. Rev. Lett. **101**, 128301 (2008).

[5] E. Eriksson, J. Enger, B. Nordlander, N. Erjavec, K. Ramser, M. Goksör, S. Hohmann, T. Nyström, and D. Hanstorp, A microfluidic system in combination with optical tweezers for analyzing rapid and reversible cytological

alterations in single cells upon environmental changes, Lab Chip **7**, 71 (2007).

[6] K. C. Neuman and S. M. Block, Optical trapping, Rev. Sci. Instrum **75**, 2787 (2004).

[7] I. A. Favre-Bulle, A. B. Stilgoe, E. K. Scott, and H. Rubinsztein-Dunlop, Optical trapping in vivo: Theory, practice, and applications, Nanophotonics **8**, 1023 (2019).

[8] D. Gao, W. Ding, M. Nieto-Vesperinas, X. Ding, M. Rahman, T. Zhang, C. Lim, and C. W. Qiu, Optical manipulation from the microscale to the nanoscale: Fundamentals, advances and prospects, Light Sci. Appl. **6**, e17039 (2017).

[9] P. C. Chaumet, A. Rahmani, and M. Nieto-Vesperinas, Optical Trapping and Manipulation of Nano-Objects with an Apertureless Probe, Phys. Rev. Lett. **88**, 123601 (2002).

[10] H. Furukawa and I. Yamaguchi, Optical trapping of metallic particles by a fixed Gaussian beam, Opt. Lett. **23**, 216 (1998).

[11] A. Ashkin, J. M. Dziedzic, and T. Yamane, Optical trapping and manipulation of single cells using infrared laser beams, Nature **330**, 769 (1987).

[12] A. Ashkin, J. M. Dziedzic, J. E. Bjorkholm, and S. Chu, Observation of a single-beam gradient force optical trap for dielectric particles, Opt. Lett. **11**, 288 (1986).

[13] A. Ashkin, Optical trapping and manipulation of neutral particles using lasers, Proc. Natl. Acad. Sci. **94**, 4853 (1997).

[14] P. C. Chaumet and M. Nieto-Vesperinas, Time-averaged total force on a dipolar sphere in an electromagnetic field, Opt. Lett. **25**, 1065 (2000).

[15] G. Volpe, L. Helden, T. Brettschneider, J. Wehr, and C. Bechinger, Influence of Noise on Force Measurements, Phys. Rev. Lett. **104**, 170602 (2010).

[16] M. G. Silveirinha, S. A. H. Gangaraj, G. W. Hanson, and M. Antezza, Fluctuation-induced forces on an atom near a photonic topological material, Phys. Rev. A. **97**, 022509 (2018).

[17] M. L. Juan, M. Righini, and R. Quidant, Plasmon nano-optical tweezers, Nat. Photonics **5**, 349 (2011).

[18] M. Righini, G. Volpe, C. Girard, D. Petrov, and R. Quidant, Surface Plasmon Optical Tweezers: Tunable Optical Manipulation in the Femtonewton Range, Phys. Rev. Lett. **100**, 186804 (2008).

[19] Y. Tsuboi, T. Shoji, N. Kitamura, M. Takase, K. Murakoshi, Y. Mizumoto, and H. Ishihara, Optical trapping of quantum dots based on gap-mode-excitation of localized surface plasmon, J. Phys. Chem. Lett. **1**, 2327 (2010).

[20] K. Wang, E. Schonbrun, P. Steinvurzel, and K. B. Crozier, Trapping and rotating nanoparticles using a plasmonic nano-tweezer with an integrated heat sink, Nat. Commun. **2**, 469 (2011).

[21] L. Novotny and B. Hecht, *Principle of Nano-Optics* (Cambridge University Press, Cambridge, UK, 2012).

[22] F. J. Rodríguez-Fortuño, N. Engheta, A. Martínez, and A. V. Zayats, Lateral forces on circularly polarizable particles near a surface, Nat. Commun. **6**, 8799 (2015).

[23] M. I. Petrov, S. V. Sukhov, A. A. Bogdanov, A. S. Shalin, and A. Dogariu, Surface plasmon polariton assisted optical pulling force, Laser Photonics Rev. **10**, 116 (2016).

[24] J. J. Kingsley-Smith, M. F. Picardi, L. Wei, A. V. Zayats, and F. J. Rodríguez-Fortuño, Optical forces from

near-field directionalities in planar structures, Phys. Rev. B **99**, 235410 (2019).

[25] A. Ivinskaya, N. Kostina, A. Proskurin, M. I. Petrov, A. A. Bogdanov, S. Sukhov, A. V. Krasavin, A. Karabchevsky, A. S. Shalin, and P. Ginzburg, Optomechanical manipulation with hyperbolic metasurfaces, ACS Photonics **5**, 4371 (2018).

[26] S. B. Wang and C. T. Chan, Lateral optical force on chiral particles near a surface, Nat. Commun. **5**, 3307 (2014).

[27] A. Hayat, J. B. Mueller, and F. Capasso, Lateral chirality-sorting optical forces, Proc. Natl. Acad. Sci. **112**, 13190 (2015).

[28] K. Y. Bliokh, F. J. Rodríguez-Fortuño, F. Nori, and A. V. Zayats, Spin–orbit interactions of light, Nat. Photonics **9**, 796 (2015).

[29] J. Petersen, J. Volz, and A. Rauschenbeutel, Chiral nanophotonic waveguide interface based on spin-orbit interaction of light, Science **346**, 67 (2014).

[30] D. O'connor, P. Ginzburg, F. J. Rodríguez-Fortuño, G. A. Wurtz, and A. V. Zayats, Spin -orbit coupling in surface plasmon scattering by nanostructures, Nat. Commun. **5**, 5327 (2014).

[31] N. K. Paul, D. Correas-Serrano, and J. S. Gomez-Diaz, Giant lateral optical forces on Rayleigh particles near hyperbolic and extremely anisotropic metasurfaces, Phys. Rev. B. **99**, 121408 (2019).

[32] J. S. Gomez-Diaz and A. Alù, Flatland optics with hyperbolic metasurfaces, ACS Photonics **3**, 2211 (2016).

[33] J. S. T. Smalley, F. Vallini, S. A. Montoya, L. Ferrari, S. Shahin, C. T. Riley, B. Kanté, E. E. Fullerton, Z. Liu, and Y. Fainman, Luminescent hyperbolic metasurfaces, Nat. Commun. **8**, 13793 (2017).

[34] J. S. Gomez-Diaz, M. Tymchenko, and A. Alù, Hyperbolic metasurfaces: Surface plasmons, light-matter interactions, and physical implementation using graphene strips, Opt. Mater. Express **5**, 2313 (2015).

[35] J. S. Gomez-Diaz, M. Tymchenko, and A. Alù, Hyperbolic Plasmons and Topological Transitions Over Uniaxial Metasurfaces, Phys. Rev. Lett. **114**, 233901 (2015).

[36] D. Correas-Serrano, J. S. Gomez-Diaz, M. Tymchenko, and A. Alù, Nonlocal response of hyperbolic metasurfaces, Opt. Express **23**, 29434 (2015).

[37] P. Li, I. Dolado, F. J. Alfaro-Mozaz, F. Casanova, L. E. Hueso, S. Liu, J. H. Edgar, A. Y. Nikitin, S. Vélez, and R. Hillenbrand, Infrared hyperbolic metasurface based on nanostructured van der Waals materials, Science **359**, 892 (2018).

[38] A. A. High, R. C. Devlin, A. Dibos, M. Polking, D. S. Wild, J. Perczel, N. P. de Leon, M. D. Lukin, and H. Park, Visible-frequency hyperbolic metasurface, Nature **522**, 192 (2015).

[39] Y. Yermakov, D. V. Permyakov, F. V. Porubaev, P. A. Dmitriev, A. K. Samusev, I. V. Iorsh, R. Malureanu, A. V. Lavrinenko, and A. A. Bogdanov, Effective surface conductivity of optical hyperbolic metasurfaces: From far-field characterization to surface wave analysis, Sci. Rep. **8**, 14135 (2018).

[40] O. D. Miller, S. G. Johnson, and A. W. Rodriguez, Effectiveness of Thin Films in Lieu of Hyperbolic Metamaterials in the Near Field, Phys. Rev. Lett. **112**, 157402 (2017).

[41] A. Ivinskaya, M. I. Petrov, A. A. Bogdanov, I. Shishkin, P. Ginzburg, and A. S. Shalin, Plasmon-assisted optical trapping and anti-trapping, Light Sci. Appl. **6**, e16258 (2017).

[42] H. Bhatia, G. Norgard, V. Pascucci, and P. T. Bremer, The Helmholtz-Hodge decomposition—a survey, IEEE Trans. Vis. Comput. Graph **19**, 1386 (2012).

[43] www.comsol.com

[44] See Supplemental Material at https://link.aps.org/supplemental/10.1103/PhysRevApplied.15.014018 for a detailed derivation of the optical trapping forces induced on dipolar Rayleigh particles above anisotropic metasurfaces. Additional details regarding the effective medium theory of anisotropic metasurfaces, particle electromagnetic response and polarization, vertical forces, as well as the influence of the substrate, are also presented.

[45] D. V. Thourhout and J. Roles, Optomechanical device actuation through the optical gradient force, Nat. Photonics **4**, 211 (2010).

[46] J. Kumar, L. Li, X. L. Jiang, D. Y. Kim, T. S. Lee, and S. Tripathy, Gradient force: The mechanism for surface relief grating formation in azobenzene functionalized polymers, Appl. Phys. Lett. **72**, 2096 (1998).

[47] S. Nemeto, Nonparaxial Gaussian beams, Appl. Opt. **29**, 1940 (1990).

[48] G. P. Agarwal and D. N. Pattanayak, Gaussian beam propagation beyond the paraxial approximation, J. Opt. Soc. Am. A **69**, 575 (1979).

[49] A. Rohrbach, Stiffness of Optical Traps: Quantitative Agreement Between Experiment and Electromagnetic Theory, Phys. Rev. Lett. **95**, 168102 (2005).

[50] L. Novotny, R. X. Bian, and X. S. Xie, Theory of Nanometric Optical Tweezers, Phys. Rev. Lett. **79**, 645 (1997).

[51] M. A. Zaman, P. Padhy, and L. Hesselink, Near-field optical trapping in a non-conservative force field, Sci. Rep. **9**, 1 (2019).

[52] S. Sukhov and A. Dogariu, Non-conservative optical forces, Rep. Prog. Phys. **80**, 112001 (2017).

[53] M. A. Zaman, P. Padhy, and L. Hesselink, Solenoidal optical forces from a plasmonic Archimedean spiral, Phys. Rev. A **100**, 013857 (2019).

[54] D. Zill, W. S. Wright, and M. R. Cullen, *Advanced Engineering Mathematics* (Jones & Bartlett Learning, Burlington, 2011).

[55] F. Hajizadeh and S. N. S. Reihani, Optimized optical trapping of gold nanoparticles, Opt. Express **18**, 551 (2010).

[56] M. Šiler and P. Zemánek, Particle jumps between optical traps in a one-dimensional (1D) optical lattice, New J. Phys. **12**, 083001 (2010).

[57] Y. Wu, C. Zhang, N. M. Estakhri, Y. Zhao, J. Kim, M. Zhang, X. X. Liu, G. K. Pribil, A. Alù, C. K. Shih, and X. Li, Intrinsic optical properties and enhanced plasmonic response of epitaxial silver, Adv. Mater. **26**, 6106 (2014).

[58] A. Vakil and N. Engheta, Transformation optics using graphene, Science **332**, 1291 (2011).

[59] O. Y. Yermakov, A. I. Ovcharenko, M. Song, A. A. Bogdanov, I. V. Iorsh, and Y. S. Kivshar, Hybrid waves localized at hyperbolic metasurfaces, Phys. Rev. B **91**, 235423 (2015).

[60] I. Trushkov and I. Iorsh, Two-dimensional hyperbolic medium for electrons and photons based on the array of tunnel-coupled graphene nanoribbons, Phys. Rev. B **92**, 045305 (2015).

[61] A. Nemilentsau, T. Low, and G. Hanson, Anisotropic 2D Materials for Tunable Hyperbolic Plasmonics, Phys. Rev. Lett. **116**, 066804 (2016).

[62] D. Bedeaus and J. Vileger, *Optical Properties of Surfaces* (Imperial college press, London, 2004).

[63] A. V. Kildishev, A. Boltasseva, and V. M. Shalaev, Planar photonics with metasurfaces, Science **339**, 1232009 (2013).

[64] D. Correas-Serrano, J. S. Gomez-Diaz, A. A. Melcon, and A. Alù, Black phosphorus plasmonics: Anisotropic elliptical propagation and nonlocality-induced canalization, J. Opt. **18**, 104006 (2016).

[65] E. Van Veen, A. Nemilentsau, A. Kumar, R. Roldán, M. I. Katsnelson, T. Low, and S. Yuan, Tuning two-Dimensional Hyperbolic Plasmons in Black Phosphorus, Phys. Rev. Appl. **12**, 014011 (2019).

[66] C. Wang, S. Huang, Q. Xing, Y. Xie, C. Song, F. Wang, and H. Yan, Van der Waals thin films of WTe 2 for natural hyperbolic plasmonic surfaces, Nat. Commun. **11**, 1 (2020).

[67] A. J. Frenzel, C. C. Homes, Q. D. Gibson, Y. M. Shao, K. W. Post, A. Charnukha, R. J. Cava, and D. N. Basov, Anisotropic electrodynamics of type-II Weyl semimetal candidate WTe 2, Phys. Rev. B **95**, 245140 (2017).

[68] D. Correas-Serrano, A. Alù, and J. S. Gomez-Diaz, Plasmon canalization and tunneling over anisotropic metasurfaces, Phys. Rev. B **96**, 075436 (2017).

[69] J. L. Garrett, D. A. Somers, and J. N. Munday, Measurement of the Casimir Force Between Two Spheres, Phys. Rev. Lett. **120**, 040401 (2018).

[70] C. C. Homes, M. N. Ali, and R. J. Cava, Optical properties of the perfectly compensated semimetal WTe 2, Phys. Rev. B **92**, 161109 (2015).

[71] J. Sun, N. M. Litchinitser, and J. Zhou, Indefinite by nature: From ultraviolet to terahertz, ACS Photonics **1**, 293 (2014).

[72] S. Guan, S. Y. Huang, Y. Yao, and S. A. Yang, Tunable hyperbolic dispersion and negative refraction in natural electride materials, Phys. Rev. B **95**, 165436 (2017).

[73] J. D. Caldwell, A. V. Kretinin, Y. Chen, V. Giannini, M. M. Fogler, Y. Francescato, C. T. Ellis, J. G. Tischler, C. R. Woods, A. J. Giles, and M. Hong, Sub-diffractional volume-confined polaritons in the natural hyperbolic material hexagonal boron nitride, Nat. Commun. **5**, 1 (2014).

[74] S. Dai, Q. Ma, M. K. Liu, T. Andersen, Z. Fei, M. D. Goldflam, M. Wagner, K. Watanabe, T. Taniguchi, M. Thiemens, and F. Keilmann, Graphene on hexagonal boron nitride as a tunable hyperbolic metamaterial, Nat. Nanotech. **10**, 682 (2015).

[75] V. W. Brar, M. S. Jang, M. Sherrott, S. Kim, J. J. Lopez, L. B. Kim, M. Choi, and H. Atwater, Hybrid surface-phonon-plasmon polariton modes in graphene/monolayer h-BN heterostructures, Nano Lett. **14**, 3876 (2014).

[76] W. Ma, P. Alonso-González, S. Li, A. Y. Nikitin, J. Yuan, J. Martín-Sánchez, J. Taboada-Gutiérrez, I. Amenabar, P. Li, S. Vélez, and C. Tollan, In-plane anisotropic and ultra-low-loss polaritons in a natural van der Waals crystal, Nature **562**, 557 (2018).

[77] Z. Zheng, N. Xu, S. L. Oscurato, M. Tamagnone, F. Sun, Y. Jiang, Y. Ke, J. Chen, W. Huang, W. L. Wilson, and A. Ambrosio, A mid-infrared biaxial hyperbolic van der Waals crystal, Sci. Adv. **5**, eaav8690 (2019).

[78] M. N. Gjerding, R. Petersen, T. G. Pedersen, N. A. Mortensen, and K. S. Thygesen, Layered van der waals crystals with hyperbolic light dispersion, Nat. Commun. **8**, 1 (2017).